A&A, 699, A91 (2025)
https://doi.org/10.1051/0004-6361/202554182

Astronomy & Astrophysics

MOA-2022-BLG-091Lb and KMT-2024-BLG-1209Lb: Microlensing planets detected through weak caustic-crossing signals

Cheongho Han[1], Chung-Uk Lee[2,⋆], Andrzej Udalski[3], Ian A. Bond[4], Hongjing Yang[5], Michael D. Albrow[6], Sun-Ju Chung[2], Andrew Gould[7], Youn Kil Jung[2,8], Kyu-Ha Hwang[2], Yoon-Hyun Ryu[2], Yossi Shvartzvald[9], In-Gu Shin[10], Jennifer C. Yee[10], Weicheng Zang[10,5], Tanagodchaporn Inyanya[2,8], Sang-Mok Cha[2,11], Doeon Kim[1], Dong-Jin Kim[2], Seung-Lee Kim[2], Dong-Joo Lee[2], Yongseok Lee[2,11], Byeong-Gon Park[2], Richard W. Pogge[7],
(The KMTNet Collaboration)
Przemek Mróz[3], Michał K. Szymański[3], Jan Skowron[3], Radosław Poleski[3], Igor Soszyński[3], Paweł Pietrukowicz[3], Szymon Kozłowski[3], Krzysztof A. Rybicki[3,9], Patryk Iwanek[3], Krzysztof Ulaczyk[12], Marcin Wrona[3,13], Mariusz Gromadzki[3], Mateusz J. Mróz[3], Michał Jaroszyński[3], Marcin Kiraga[3],
(The OGLE Collaboration)
Fumio Abe[14], Ken Bando[15], David P. Bennett[16,17], Aparna Bhattacharya[16,17], Akihiko Fukui[18,19], Ryusei Hamada[15], Shunya Hamada[15], Naoto Hamasaki[15], Yuki Hirao[20], Stela Ishitani Silva[16,21], Naoki Koshimoto[15], Yutaka Matsubara[14], Shota Miyazaki[22], Yasushi Muraki[14], Tutumi Nagai[15], Kansuke Nunota[15], Greg Olmschenk[16], Clément Ranc[23], Nicholas J. Rattenbury[24], Yuki Satoh[15], Takahiro Sumi[15], Daisuke Suzuki[15], Sean K. Terry[16,17], Paul J. Tristram[25], Aikaterini Vandorou[16,17], Hibiki Yama[15],
(The MOA Collaboration)
Yunyi Tang[5], Shude Mao[5], Dan Maoz[26], and Wei Zhu
(The LCO Collaboration)[5]

(Affiliations can be found after the references)

Received 19 February 2025 / Accepted 28 May 2025

ABSTRACT

Aims. The light curves of the microlensing events MOA-2022-BLG-091 and KMT-2024-BLG-1209 exhibit anomalies with very similar features. These anomalies appear near the peaks of the light curves, where the magnifications are moderately high, and are distinguished by weak caustic-crossing features with minimal distortion while the source remains inside the caustic. To achieve a deeper understanding of these anomalies, we conducted a comprehensive analysis of the lensing events.

Methods. We carried out binary-lens modeling with a thorough exploration of the parameter space. This analysis revealed that the anomalies in both events are of planetary origin, although their exact interpretation is complicated by different types of degeneracy. In the case of MOA-2022-BLG-091, the main difficulty in the interpretation of the anomaly arises from a newly identified degeneracy related to the uncertain angle at which the source trajectory intersects the planet–host axis. For KMT-2024-BLG-1209, the interpretation is affected by the previously known inner-outer degeneracy, which leads to ambiguity between solutions in which the source passes through either the inner or outer caustic region relative to the planet host.

Results. Bayesian analysis indicates that the planets in both lens systems are giant planets with masses about two to four times that of Jupiter, orbiting early K-type main-sequence stars. Both systems are likely located in the Galactic disk at a distance of around 4 kiloparsecs. The degeneracy in KMT-2024-BLG-1209 is challenging to resolve because it stems from intrinsic similarities in the caustic structures of the degenerate solutions. In contrast, the degeneracy in MOA-2022-BLG-091, which occurs by chance rather than from inherent characteristics, is expected to be resolved by the future space based Roman RGES microlensing survey.

Key words. gravitational lensing: micro – planets and satellites: detection

1. Introduction

Gravitational microlensing is an important technique for detecting extrasolar planets, offering unique scientific value by enabling the discovery of planetary types that are difficult to detect using other methods (Mao & Paczyński 1991; Gould & Loeb 1992). Notably, microlensing is particularly sensitive to wide-orbit planets, which orbit their host stars at significant distances, such as OGLE-2016-BLG-1227L (Han et al. 2020), OGLE-2012-BLG-0838L (Poleski et al. 2020), and OGLE-2017-BLG-0448L (Zhai et al. 2024). It is also adept at detecting free-floating planets that are not gravitationally bound to any star, including OGLE-2012-BLG-1323L and OGLE-2017-BLG-0560L (Mróz et al. 2019), OGLE-2019-BLG-0551L (Mróz et al. 2020), OGLE-2016-BLG-1540L (Mróz et al. 2018), KMT-2019-BLG-2073L (Kim et al. 2021), and KMT-2023-BLG-2669L (Jung et al. 2024). By revealing these elusive objects, microlensing plays a pivotal role in advancing our understanding of planetary demographics and complements the discoveries made by other detection techniques.

⋆ Corresponding author: leecu@kasi.re.kr

Currently, planetary microlensing surveys are being conducted by three major groups: the Optical Gravitational Lensing Experiment (OGLE; Udalski et al. 2015), the Microlensing Observations in Astrophysics (MOA; Bond et al. 2001; Sumi et al. 2003), and the Korea Microlensing Telescope Network (KMTNet; Kim et al. 2016). These surveys utilize a network of 1-meter-class ground-based telescopes equipped with wide-field cameras, strategically distributed across multiple locations in the Southern Hemisphere. By concentrating on the densely populated stellar regions near the Galactic center, they detect microlensing events and identify planetary signals embedded within the light curves of these events. Collectively, these efforts yield approximately 30 planetary discoveries annually (Gould et al. 2022), making microlensing the third most productive planet detection method, after the transit and radial velocity techniques.

Gravitational microlensing surveys are planned to undergo further expansion. One is the PRime-focus Infrared Microlensing Experiment (PRIME), a recently completed project currently undergoing test observations. This survey aims to conduct a dedicated near-infrared microlensing survey using a 1.8-meter telescope with a wide field of view of 1.45 square degrees, located at the South African Astronomical Observatory. Its primary goal is to observe the central bulge region of the Milky Way, where high extinction makes optical observations challenging. The PRIME survey is expected to detect 42–52 planets annually, including 1–2 planets with masses below that of Earth, offering a significant contribution to the study of planetary demographics in the high-extinction regions of our galaxy (Kondo et al. 2023).

The Nancy Grace Roman Space Telescope (Roman) is set to conduct the Galactic Exoplanet Survey (RGES) from space, employing the microlensing method to discover planets. The planned survey area spans approximately 2 square degrees near the Galactic bulge, utilizing the telescope's wide 1–2 μm W146 filter with a 15-minute observational cadence. Over the course of six 72-day observing seasons, the RGES is expected to identify around 1400 bound exoplanets with masses exceeding ~0.1 Earth masses, including approximately 200 planets with masses less than 3 Earth masses (Penny et al. 2019). Additionally, Roman will detect roughly 250 free-floating planets, with masses as low as that of Mars, including about 60 planets with masses below Earth mass (Johnson et al. 2020).

In gravitational microlensing light curves, planets appear as a range of distinctive signal patterns. These planetary signals are generated when a source star passes through the perturbation region created by the caustic, which is induced by the gravitational influence of a planet. The size and shape of the caustic vary depending on the separation between the planet and its host star, as well as the mass ratio of the two. As a result, the planetary signals can take on a variety of forms, depending on the planet's position and mass in relation to its host star. Furthermore, the pattern of the planetary signal further varies depending on the path the source star takes relative to the caustic, adding more complexity to the observed light curve.

As the discovery of microlensing planets increases, instances of planets exhibiting similar signal patterns are being identified. For example, Han et al. (2025) identified planets by analyzing three lensing events MOA-2022-BLG-033, KMT-2023-BLG-0119, and KMT-2023-BLG-1896 that displayed common short-term dip features near the peaks of highly magnified lensing light curves. Another group of planetary events with similar signal characteristics, reported by Han et al. (2024a), includes KMT-2020-BLG-0757Lb, KMT-2022-BLG-0732Lb, KMT-2022-BLG-1787Lb, and KMT-2022-BLG-1852Lb. In these cases, the planetary signals appeared as extended negative deviations on the wings of the lensing light curves. Additionally, Han et al. (2024b) presented analyses on the light curves of two planetary events KMT-2021-BLG-2609 and KMT-2022-BLG-0303, for which the planetary signals appeared as as positive deviations on the wings of lensing light curves. Planetary events with similar traits were reported by Jung et al. (2021) for the lensing events OGLE-2018-BLG-0567 and OGLE-2018-BLG-0962 and by Ryu et al. (2024) for events OGLE-2017-BLG-1777 and OGLE-2017-BLG-0543. Studying planetary lensing events that show similar signal patterns is not only important for understanding the mechanisms behind these signals but also essential for identifying similar planetary signals in future discoveries.

In this paper, we analyze two microlensing events, MOA-2022-BLG-091 and KMT-2024-BLG-1209, which display anomalies with closely similar patterns. We investigate the origins of these anomalies and the degeneracies that complicate their interpretation. The structure of this paper is as follows. In Sect. 2, we outline the data used in our analyses, including details of the observations, the data reduction process, and the instrument specifications. Sect. 3 provides a brief overview of the fundamentals of planetary microlensing and describes the modeling procedure employed. The results for each event are presented in detail in the subsequent sections: Sect. 4 focuses on MOA-2022-BLG-091, while Sect. 5 discusses KMT-2024-BLG-1209. In Sect. 6, we identify the source stars for each event and estimate the angular radius of the Einstein ring. In Sect. 7, we describe the Bayesian analyses conducted to derive the physical parameters of the lenses and present these parameters. Finally, in Sect. 8, we summarize the findings and conclude our study.

2. Observations and data

The planetary signals in the two lensing events were initially identified through an inspection of the light curves of KMTNet events KMT-2022-BLG-0114 and KMT-2024-BLG-1209. A subsequent review of data from other microlensing surveys revealed that KMT-2022-BLG-0114 was also observed by the MOA survey, where it is designated as MOA-2022-BLG-091, while KMT-2024-BLG-1209 was additionally observed by the OGLE survey and designated as OGLE-2024-BLG-0777. Moreover, follow-up observations using two telescopes from the Las Cumbres Observatory (LCO) global telescope network covered the peak region of KMT-2024-BLG-1209. Our analysis is based on the combined datasets from these observations.

The event KMT-2022-BLG-0114 was announced by the KMTNet survey on March 23, 2022, while the MOA survey issued an alert earlier, on March 14, 2022. For KMT-2024-BLG-1209, the KMTNet survey issued an alert on March 31, 2024, followed by the OGLE survey on June 17, 2024. When an event is observed by multiple surveys, it is customary to adopt the event ID designated by the group that first discovered it. Therefore, we designate the events as MOA-2022-BLG-091 and KMT-2024-BLG-1209 throughout this work. Table 1 provides the equatorial and Galactic coordinates of the events along with their corresponding survey designations.

The three optical lensing surveys were conducted using multiple telescopes distributed across the Southern Hemisphere. The KMTNet survey operates three identical telescopes, located at the Siding Spring Observatory in Australia (KMTA), the Cerro Tololo Inter-American Observatory in Chile (KMTC), and the South African Astronomical Observatory in South Africa (KMTS). Each telescope has a 1.6-meter aperture and is equipped with a camera that provides a 4-square-degree field

Table 1. Event coordinates and correspondence.

Event	$(\mathrm{RA, Dec})_{\mathrm{J2000}}$	(l, b)	Other reference
MOA-2022-BLG-091	(17:55:46.13, –32:20:29.18)	(−1°.8118, −3°.616)	KMT-2022-BLG-0114
KMT-2024-BLG-1209	(17:26:27.11, –28:07:14.02)	(−1°.5803, 3°.9868)	OGLE-2024-BLG-0777

of view. The OGLE survey uses a 1.3-meter telescope at Las Campanas Observatory in Chile, equipped with a camera that provides a 1.4-square-degree field of view. The MOA survey operates a 1.8-meter telescope at Mt. John University Observatory in New Zealand, which is fit with a camera covering a 2.2-square-degree field of view. The LCO data covering the peak region of KMT-2024-BLG-1209 were taken using the 1.0 m telescopes from the Siding Spring Observatory in Australia (LCOA) and the Cerro Tololo Inter-American Observatory in Chile (LCOC). Images from these followup observations were taken in the I band.

Images from the KMTNet and OGLE surveys were primarily taken in the I band, while those from the MOA survey were captured in the customized MOA-R band, which covers a wavelength range of 609–1109 nm. A subset of images from all three surveys was taken in the V band to measure the source colors of the events. Image reduction and photometry for the microlensing events were conducted using the pipelines developed by the respective survey groups: the KMTNet data were processed with the pipeline from Albrow et al. (2009), the OGLE data with the pipeline from Udalski (2003), and the MOA data with the pipeline described by Bond et al. (2001). For the KMTNet and LCO data sets, we performed additional photometry using the code developed by Yang et al. (2024) to ensure optimal data quality. For each dataset, we adjusted the error bars to achieve two objectives: first, they were consistent with the data scatter, and second, the value of χ^2 per degree of freedom was equal to unity. This error bar normalization followed the procedure outlined in Yee et al. (2012).

3. Fundamentals of planetary lensing and modeling

A planet-induced caustic take different shape and appears at different locations depending on the projected separation from the host to the planet and the planet/star mass ratio (Gaudi 2012). When the planet/star mass ratio is very small and the planet lies away from the Einstein ring, the planet forms two sets of caustics. One tiny caustic is located near the host star (central caustic), and the other is positioned at a position of $\mathbf{u}_{\mathrm{c}} = \mathbf{s} - 1/\mathbf{s}$ from the star (peripheral caustic). Here, $\mathbf{s}$ denotes the position vector of the planet relative to its host, with its length scaled to the angular Einstein radius θ_{E}. When $s > 1$ (wide planet), $u_{\mathrm{c}} > 0$, and a peripheral caustic is located in the region between the star and the planet. On the other hand, when $s < 1$ (close planet), $u_{\mathrm{c}} < 0$, and peripheral caustics are located on the opposite side of the planet relative to the star. A wide planet creates a single four-cusp peripheral caustic, while a close planet creates two three-cusp caustics. For further details on the variation in caustics with respect to planetary separation and mass ratio, refer to Han (2006) for peripheral caustics and Chung et al. (2005) for central caustics.

For giant planets with mass ratios on the order of 10^{-3} and located near the Einstein ring of their host stars, the central and planetary caustics merge into a single, large "resonant" caustic. This caustic forms a closed curve consisting of six concave segments that meet at six cusps. The cusps aligned along the planet-host axis are strong, producing significant deviations when the source passes through this region. In contrast, the cusps oriented perpendicular to the axis are weaker, resulting in relatively small perturbations when the source crosses these areas.

Modeling of the light curves was performed to determine a lensing solution, representing the set of lensing parameters that best account for the observed anomalies. For a lensing event in which the lens is composed of two masses and the source is a single star (2L1S event), the lensing light curve is described by seven basic parameters. The first three parameters $(t_0, u_0, t_{\mathrm{E}})$ describe the lens-source approach. Specifically, t_0 represents the time of closest approach, u_0 denotes the lens-source separation at that moment (scaled to θ_{E}), and t_{E} is the event timescale, defined as the time required for the source to traverse θ_{E}. Two additional parameters, (s, q), represent the projected separation and mass ratio between the binary lens components, respectively, and define the binary lens. Another parameter, α, denotes the source incidence angle, which is the angle between the direction of the source's motion and the binary lens axis. Finally, the normalized source radius, ρ, is required to characterize the finite lensing magnifications during the source's crossing or close approach to the caustic.

Modeling was performed using a combination of grid and downhill methods. For the lensing parameters (s, q), where the magnification changes discontinuously with variations in these parameters, we used a grid approach with multiple initial values of α. The initial parameter ranges explored in the grid search were set to $-1.0 \le \log s \le 1.0$ and $-5.0 \le \log q \le 1.0$, and were subsequently refined in a stepwise manner. For the source trajectory angle, 25 initial values uniformly spaced over the range from 0 to 2π. For the remaining parameters, where the magnification changes smoothly, we applied a downhill method. In the downhill approach, the Markov Chain Monte Carlo (MCMC) method was applied. In the first round of modeling, we constructed a χ^2 map on the s–q–α parameter planes to examine potential degenerate solutions. We then refined the individual local solutions by allowing all parameters to vary. To assess the severity of the degeneracy, we compared the χ^2 values of the fits for the local solutions. If the degeneracy was significant, we presented all local solutions and investigated the underlying causes of the degeneracies. In the following sections, we present the result of analyses for the individual events.

4. MOA-2022-BLG-091

Figure 1 shows the lensing light curve of the event MOA-2022-BLG-091. The event reached a moderately high magnification of $A_{\mathrm{max}} \sim 31$ at the peak. At first glance, the light curve appears to be that of a single-lens single-source (1L1S) event with a smooth and symmetric shape. However, upon closer inspection, we observed a weak deviation in the light curve. The upper panel presents a close-up view of the peak region, illustrating that the

Table 2. Lensing parameters of four degenerate solutions of MOA-2022-BLG-091.

Parameter	Sol A	Sol B	Sol C	Sol D
χ^2	1727.8	1726.7	1733.4	1731.7
t_0 (HJD′)	9657.729 ± 0.012	9657.785 ± 0.017	9657.699 ± 0.0127	9657.706 ± 0.008
u_0 (10^{-2})	2.565 ± 0.080	2.614 ± 0.087	2.642 ± 0.084	2.590 ± 0.84
t_E (days)	34.68 ± 0.86	34.51 ± 0.89	34.53 ± 0.87	34.54 ± 0.85
s	1.0029 ± 0.0025	1.0033 ± 0.0023	1.0132 ± 0.0006	1.0195 ± 0.0027
q (10^{-3})	4.55 ± 0.48	4.36 ± 0.28	3.38 ± 0.31	4.10 ± 0.55
α (rad)	4.632 ± 0.018	4.354 ± 0.073	4.811 ± 0.034	4.745 ± 0.004
ρ (10^{-3})	<1.5	<1.5	<1.5	<1.5

Notes. HJD′ = HJD − 2 450 000.

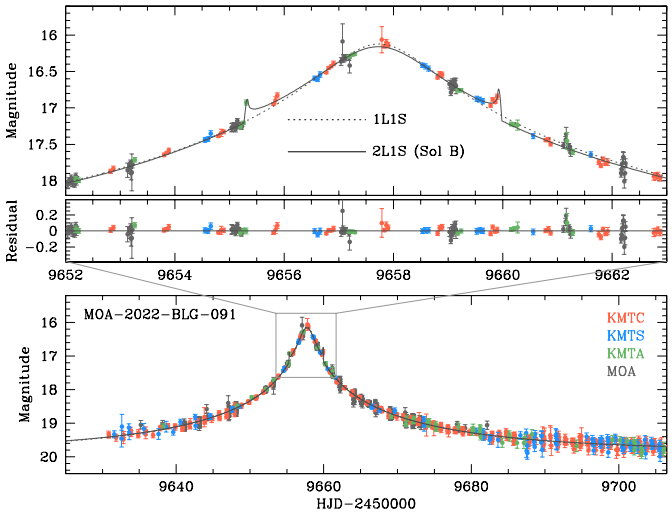

Fig. 1. Light curve of lensing event MOA-2022-BLG-091. The lower panel displays the full light curve, while the upper panels provide a zoomed-in view of the region around the peak. The dotted and solid curves overlaid on the data points represent the 1L1S model and one of the 2L1S models (solution B), respectively. The middle panel shows the residuals from the 2L1S solution. The colors of the data points are selected to correspond with the legends.

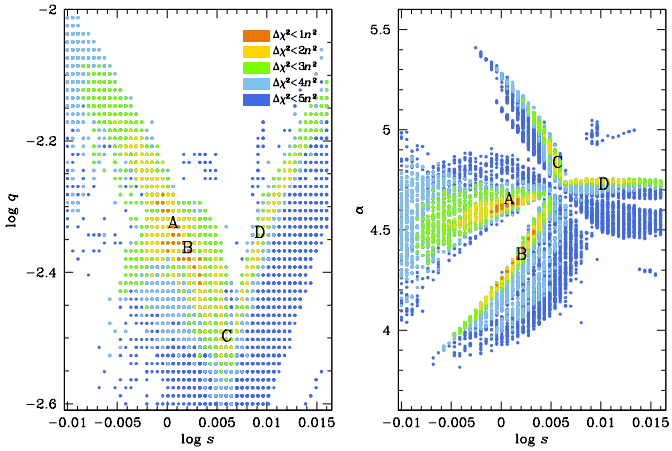

Fig. 2. Locations of four degenerate solutions of MOA-2022-BLG-091 in the $\Delta\chi^2$ maps on the log s–log q (left panel) and log s–α (right panel) parameter planes. The color coding represents regions with $\Delta\chi^2 < 1n^2$ (red), $\Delta\chi^2 < 2n^2$ (yellow), $\Delta\chi^2 < 3n^2$ (green), $\Delta\chi^2 < 4n^2$ (cyan), and $\Delta\chi^2 < 5n^2$ (blue), where $n = 2$.

light curve deviates from the 1L1S model (dotted curve), which was derived by excluding the data points near the anomaly.

The most noticeable deviations in the light curve occurred in two distinct regions: around HJD ∼ 2459655.3, approximately 2.4 days before the peak, and around HJD ∼ 2459659.8, about 2.1 days after the peak. The time interval between these two anomalies is roughly 4.5 days. The first deviation was recorded by a single KMTA data point, while the second was captured by four KMTC data points. In both cases, the lensing magnifications exhibit abrupt variations, suggesting that the anomalies may have been caused by the source's caustic crossings. However, unlike typical caustic crossings, where deformations occur both when the source crosses caustics and when it is inside the caustic, for example, the planet-induced anomaly in the light curve of the lensing event KMT-2021-BLG-1150 (Han et al. 2023), there is little deviation in the region between the caustic spikes. This results in anomaly characteristics that differ from the typical case.

Modeling of the light curve indicated that the anomaly was produced by a planetary companion to the lens, although the interpretation is complicated by the existence of multiple possible solutions. We identified four degenerate solutions, which were labeled as "Sol A," "Sol B," "Sol C," and "Sol D." Figure 2 shows the locations of these solutions in the $\Delta\chi^2$ maps on the log s–log q (left panel) and log s–α (right panel) parameter planes. Among these, Sol B provides the best fit, but the χ^2 differences among the solutions are less than 6.7, indicating a strong degeneracy among them. Figure 3 displays the model curves of the four solutions in the region of the anomaly, illustrating that all solutions reproduce the anomaly with nearly equal accuracy.

The complete sets of lensing parameters for each solution, along with the corresponding χ^2 values of the fits, are provided in Table 2. Among these solutions, Sol C has a mass ratio of $q \sim 3.4 \times 10^{-3}$, which is smaller than the mass ratios of the other solutions, which range from $q \sim 4.1 \times 10^{-3}$ to $q \sim 4.6 \times 10^{-3}$. Although the mass ratios show slight variations, all are several times greater than the Jupiter/Sun mass ratio, indicating that the companion to the lens is a planetary mass object. The planet-host separations for all solutions are close to $s = 1$, implying that the planet is located near the Einstein ring of the primary lens. The event timescales, $t_E \sim 35$ days, are consistent across the solutions. One key distinguishing feature of the solutions is the source incidence angle, which ranges from 3.4 to 4.6 radians. Due to limited coverage of the caustic crossings, the exact value of the normalized source radius could not be determined, and only an upper limit of $\rho_{max} \sim 1.5 \times 10^{-3}$ can be established.

To understand the cause of the degeneracies among the solutions, we examined the lens system configurations. Figure 4

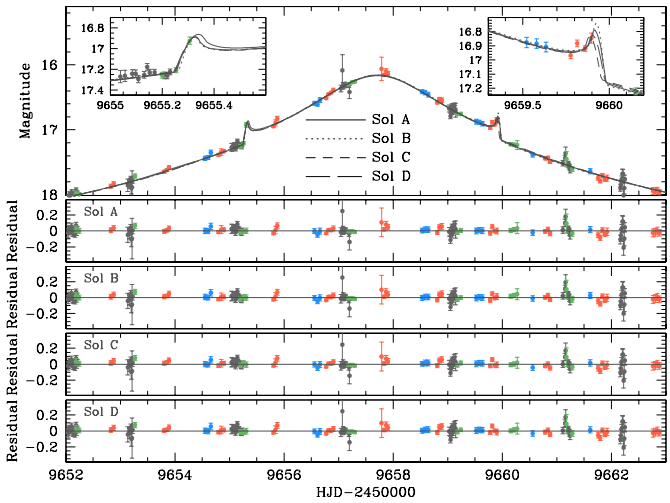

Fig. 3. Model curves of MOA-2022-BLG-091 in the region around the anomaly. The insets in the top panel provide blowup of the regions around the anomalies induced by the source's caustic crossings. The lower panels present the residuals corresponding to the four solutions.

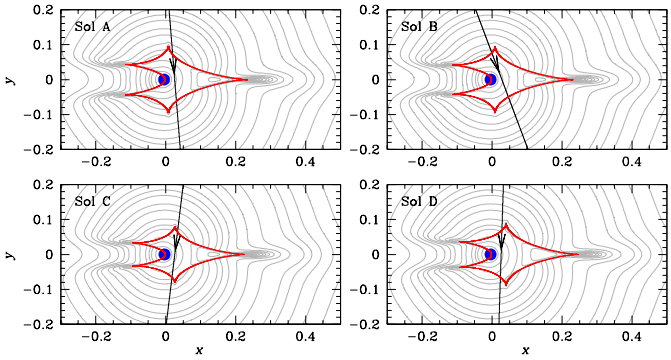

Fig. 4. Configurations of lens system for the four degenerate solutions of MOA-2022-BLG-091. In each panel, the cuspy closed curve represents the caustic, while the arrowed line denotes the source trajectory. The gray contours surrounding the caustic represent equi-magnification contours. The blue filled circle presents the location of the planet host.

shows these configurations, where the red cusped shape represents the caustic, the blue filled circle marks the position of the planet host, and the arrowed line indicates the source trajectory. All solutions form a single resonant caustic, which appears similar due to the comparable values of s and q across the solutions. The primary differences arise from the source trajectories. In Sol A, the source crosses to the right of both the upper and lower cusps of the caustic, while in Sol D, it crosses to the left of both cusps. For Sol B, the source trajectory passes to the left of the upper cusp and the right of the lower cusp, while for Sol C, the source passes to the right of the upper cusp and the left of the lower cusp. This degeneracy represents a previously unrecognized type that has not been observed in earlier interpretations of planetary signals. Therefore, it is important to consider this degeneracy when analyzing similar planetary perturbations in future events.

Since the similarities among the model light curves result from chance rather than intrinsic similarities in the caustic structures of specific lens configurations, the degeneracies could have been lifted under more favorable observational conditions. In this event, the KMTNet survey operated with a 1.0-hour cadence, in contrast to the 15-minute cadence of the Roman RGES survey.

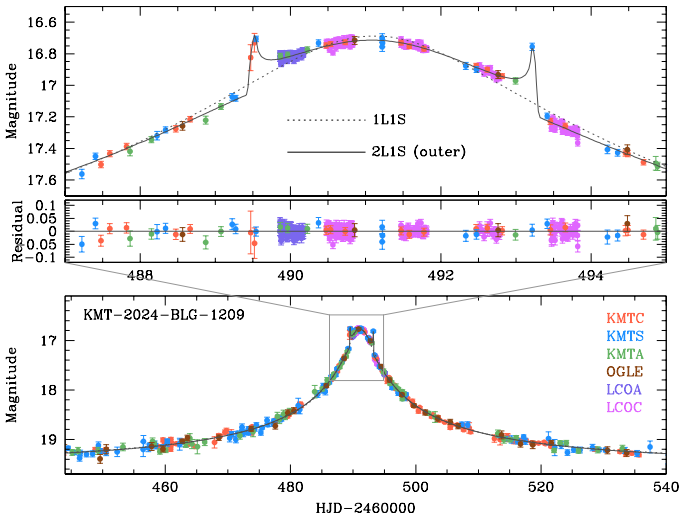

Fig. 5. Light curve of the lensing event KMT-2024-BLG-1209. Notations are same as those in Fig. 1.

Given the high photometric precision of space-based observations, such degeneracies are expected to be resolved in the RGES survey.

5. KMT-2024-BLG-1209

The lensing light curve of KMT-2024-BLG-1209 is shown in Figure 5. A closer inspection of the peak region revealed an anomaly characterized by two caustic spikes: the first occurred before the peak at HJD ~ 2460489.5, and the second occurred after the peak at HJD ~ 2460492.2, with an approximate time gap of 2.7 days between them. The event reached a moderately high magnification of $A_{\rm max} \sim 45$ at its peak. While the anomaly in KMT-2024-BLG-1209 is more pronounced than the subtle anomaly in MOA-2022-BLG-091, the two events share several similarities. First, both events exhibit weak caustic-crossing signatures, occurring before and after the peak, respectively. Second, both events reach moderately high magnifications at their peaks, and the region between the caustic spikes shows little deviation.

Given the similarities in the anomaly characteristics, we model the light curve of KMT-2024-BLG-1209 using a 2L1S configuration. We identified two local solutions, with the degeneracy between them stemming from a different origin compared to MOA-2022-BLG-091. Figure 6 shows the locations of the two local solutions in the $\Delta\chi^2$ maps on the parameter space. These solutions are designated as "inner" and "outer," with the reasoning for these labels provided below.

The complete sets of lensing parameters for both solutions, along with the corresponding χ^2 values, are presented in Table 3. For the inner solution, the binary lens parameters are $(s, q)_{\rm in} \sim (1.06, 3.33 \times 10^{-3})$, while for the outer solution, the parameters are $(s, q)_{\rm out} \sim (0.97, 2.90 \times 10^{-3})$. The degeneracy is significant, with $\Delta\chi^2 = 2.0$. The mass ratio, which is slightly more than three times that of Jupiter to the Sun, suggests that the lens companion lies in the planetary mass regime. Given the relatively long timescale of the event, we examined the possibility of detecting microlens parallax effects caused by Earth's orbital motion around the Sun (Gould 1992). However, securely measuring the microlens parallax was challenging, primarily due to significant photometric uncertainties at low magnifications.

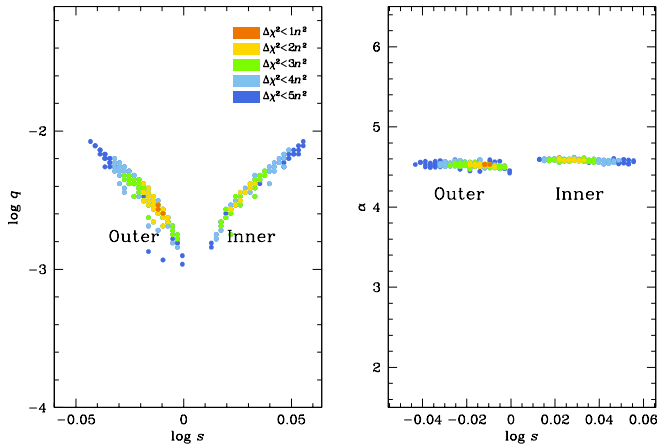

Fig. 6. $\Delta\chi^2$ maps on the log s–log q (left panel) and log s–α for KMT-2024-BLG-1209. Notations are same as those in Fig. 2.

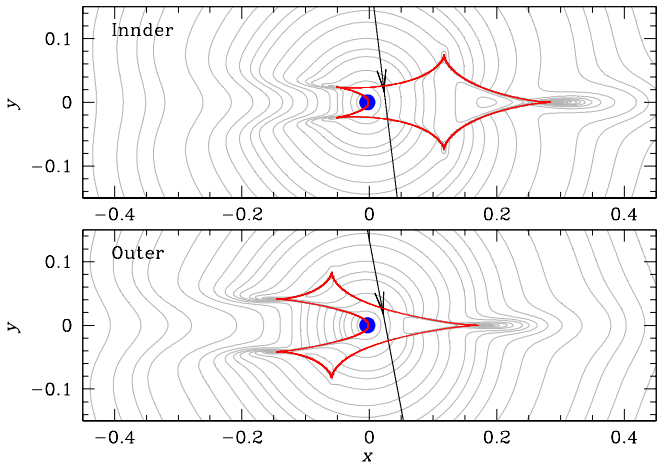

Fig. 7. Lens system configurations for the two degenerate solutions of KMT-2024-BLG-1209. Notations are same as those in Fig. 4.

Table 3. Lensing parameters of two solutions of KMT-2024-BLG-1209.

Parameter	Inner	Outer
χ^2	1731.3	1729.3
t_0 (HJD′)	491.126 ± 0.009	491.141 ± 0.007
u_0 (10^{-2})	2.57 ± 0.14	2.49 ± 0.14
$t_{\rm E}$ (days)	70.11 ± 3.77	73.13 ± 3.81
s	1.0599 ± 0.0036	0.9724 ± 0.0034
q (10^{-3})	3.33 ± 0.29	2.90 ± 0.24
α (rad)	4.5957 ± 0.0066	4.5294 ± 0.0083
ρ (10^{-3})	0.75 ± 0.20	0.73 ± 0.14

Notes. HJD′ = HJD − 2 460 000.

To understand the cause of the degeneracy between the two solutions, we compared their lens system configurations, as depicted in Figure 7. Both solutions produce a single resonant caustic, but the shapes differ. In the inner solution, the caustic appears to result from the merger of the planetary caustic on the planet side, generated by a wide planet, with the central caustic. In contrast, the outer solution's caustic seems to form from the combination of two planetary caustics on the opposite side of the planet, created by a close planet, along with the central caustic. In the inner solution, the source crosses the inner region of the planetary caustic relative to the planet host, while in the outer solution, the source passes through the outer region of the planetary caustic. Based on this distinction, we have labeled the solutions as the "inner" and "outer" solutions (Gaudi & Gould 1997). The normalized source radius, 0.8×10^{-3}, was determined from the relatively well-covered caustic region, and the measured event timescale is approximately $t_{\rm E} \sim 72$ days.

The similarity between the two model curves arises due to the inner-outer degeneracy. This is evidenced by the fact that the planet separations of the inner ($s_{\rm in}$) and outer ($s_{\rm out}$) solutions satisfy the following relation (Hwang et al. 2022; Gould et al. 2022):

$$\langle s \rangle = s^\dagger; \quad \langle s \rangle = \sqrt{s_{\rm in} \times s_{\rm out}}, \quad s^\dagger = \frac{1}{2}\left(\sqrt{u_{\rm anom}^2 + 4} \pm u_{\rm anom} \right). \quad (1)$$

Here, $\langle s \rangle$ represents the geometric mean of $s_{\rm in}$ and $s_{\rm out}$, $u_{\rm anom}^2 = \tau^2 + u_0^2$, $\tau_{\rm anom} = (t - t_{\rm anom})/t_{\rm E}$, and $t_{\rm anom}$ denotes the time of the anomaly. The sign in the last term is "+" for a positive anomaly and "−" for a negative anomaly. For KMT-2024-BLG-1209, the planet induced a positive deviation, and therefore the sign is "+". For the values $(s_{\rm in}, s_{\rm out}) = (1.0596, 0.9699)$, we calculate the geometric mean $\langle s \rangle = 1.014$. Using the parameters $(t_0, u_0, t_{\rm E}, t_{\rm anom}) \sim (491.142, 0.0248, 72.363, 491.0)$, we obtain $s^\dagger = 1.013$. The close agreement between the values of $\langle s \rangle$ and $s^\dagger$ confirms that the similarity between the model curves of the two solutions is a result of the inner-outer degeneracy.

6. Source stars and angular Einstein radii

In this section, we define the source stars for the events. Identifying the source is crucial not only for fully characterizing the event but also for determining the angular Einstein radius. The angular Einstein radius is related to the angular source radius, θ_*, through the relation

$$\theta_{\rm E} = \frac{\theta_*}{\rho}, \quad (2)$$

where θ_* is inferred from the source type, and the normalized source radius, ρ, is measured through modeling.

To determine the source type, we first estimated the source color, $(V - I)$. As an initial step, we measured the instrumental V- and I-band magnitudes by fitting the light curves in the respective passbands to the lensing model. For this measurement, we utilized photometric data processed with the pyDIA code (Albrow et al. 2017). Figure 8 presents the positions of the source stars in the instrumental color-magnitude diagrams (CMDs) for nearby stars around the sources of MOA-2022-BLG-091 (left panel) and KMT-2024-BLG-1209 (right panel). The CMDs were constructed using the pyDIA code, which was also employed to measure the source magnitudes. To minimize the spatial variation in extinction the CMDs were constructed for stars lying within 1.7 arcmin from the source. Table 4 provides the measured instrumental color and magnitude of the source star, $(V - I, I)_{\rm S}$. The uncertainties of the source color and magnitude are estimated by considering the uncertainty of the RGC position, $\sigma(V - I, I)_{\rm RGC} = (0.04, 0.02)$ (Bensby et al. 2013; Nataf et al. 2013).

In the second step, we calibrated the source color and magnitude using the red giant clump (RGC) centroid in the CMD as a reference (Yoo et al. 2004). The RGC centroid was chosen as the reference because its intrinsic (dereddened) color

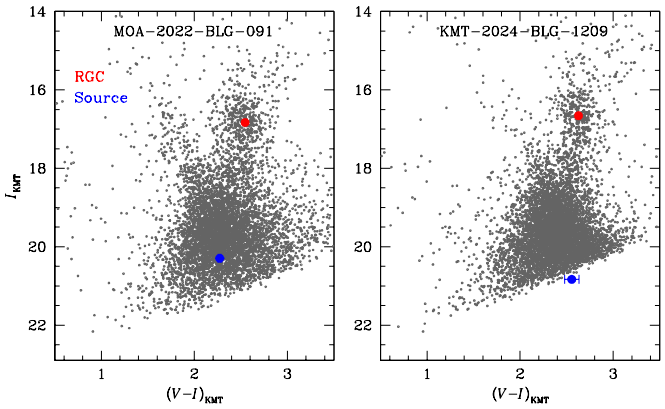

Fig. 8. Locations of source stars (blue filled dots) in the instrumental color-magnitude diagrams for nearby stars around the source stars of MOA-2022-BLG-091 (left panel) and KMT-2024-BLG-1209 (right panel). Also marked are the centroids of red giant clump (RGC, red filled dots) used for magnitude calibration.

Table 4. Source parameters and angular Einstein radii.

Parameter	MOA-2022-BLG-091	KMT-2024-BLG-1209
$(V-I)_S$	2.272 ± 0.015	2.554 ± 0.078
I_S	20.295 ± 0.002	20.833 ± 0.003
$(V-I, I)_{RGC}$	(2.545, 16.833)	(2.627, 16.660)
$I_{RGC,0}$	14.339	14.533
$(V-I)_{S,0}$	0.787 ± 0.043	0.987 ± 0.087
$I_{S,0}$	17.801 ± 0.020	18.705 ± 0.020
Type	G8V	K3V
θ_* (μas)	0.945 ± 0.077	0.783 ± 0.089
θ_E (mas)	>0.63	1.133 ± 0.378
μ (mas/yr)	>6.63	5.63 ± 1.88

Notes. $(V-I)_{RGC,0} = 1.016$.

and magnitude, $(V-I, I)_{RGC,0}$, have been well established in previous studies (Bensby et al. 2013; Nataf et al. 2013). The dereddened source color and magnitude, $(V-I, I)_{S,0}$, were then determined by applying the measured offsets in color and magnitude, $\Delta(V-I, I)$, between the source and the RGC centroid in the CMD, following the relation

$$(V-I, I)_{S,0} = (V-I, I)_{RGC,0} + \Delta(V-I, I). \quad (3)$$

Table 4 presents the estimated values of $(V-I, I)_{S,0}$ along with $(V-I, I)_{RGC}$ and $(V-I, I)_{RGC,0}$. The results indicate that the source of MOA-2022-BLG-091 is a late G-type main-sequence star, while the source of KMT-2024-BLG-1209 is an early K-type main-sequence star.

Using the measured color and magnitude, we estimated the angular source radius. To achieve this, we first converted the $V-I$ color into the $V-K$ color using the color-color relation from Bessell & Brett (1988). We then derived the angular source radius, θ_*, from the Kervella et al. (2004) relation between $(V-K, I)$ and θ_*. With the estimated angular source radius, we proceeded to estimate the angular Einstein radius, θ_E, using the relation in Eq. (2). Additionally, we calculated the relative lens-source proper motion using the relation $\mu = \theta_E/t_E$. In Table 4, we present the estimated values of θ_*, θ_E, and μ for the events. For event MOA-2022-BLG-091, where only the upper limit of the normalized source radius was constrained, we provide the lower limits for θ_E and μ.

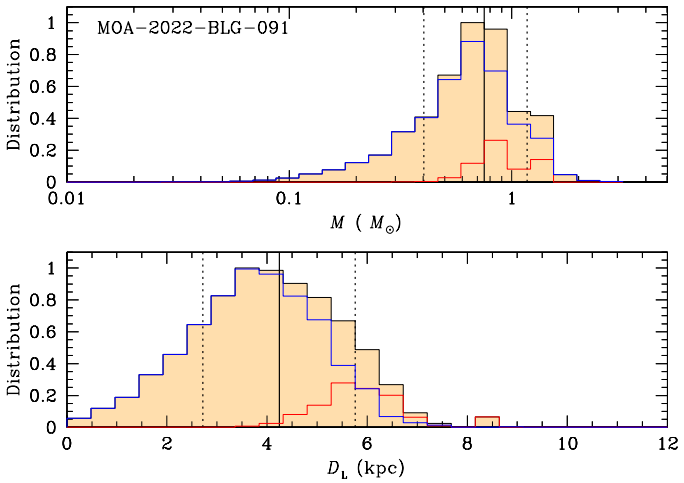

Fig. 9. Bayesian posteriors of the lens mass (upper panel) and distance (lower panel) for MOA-2022-BLG-091. In each panel, the solid vertical line represents the median of the posterior distribution, while the two dotted lines mark the 16th and 84th percentiles of the distribution. The contributions of the disk and bulge lens populations are shown separately as blue and red curves, respectively.

7. Physical lens parameters

We estimated the physical parameters of the lens mass (M) and distance (D_L) through a Bayesian analysis. This analysis incorporated constraints from the lensing observables, combined with priors from the lens mass function and the Galactic model. For the events under consideration, the lensing observables that provide information on the physical lens parameters include the event timescale and the angular Einstein radius. These quantities are related to the physical parameters through the expression:

$$t_E = \frac{\theta_E}{\mu}; \qquad \theta_E = \sqrt{\kappa M \pi_{rel}}. \quad (4)$$

Here $\kappa = 4G/(c^2\mathrm{AU})$, $\pi_{rel} = \pi_L - \pi_S = \mathrm{AU}(D_L^{-1} - D_S^{-1})$, with D_S representing the distance to the source.

The Bayesian analysis begins by generating a large number of synthetic events through a Monte Carlo simulation. For each simulated event, the physical parameters $(M_i, D_{L,i}, \mu)$ were assigned based on the lens mass function and the Galactic model, which define the physical and dynamical distributions of the lens and source. In this simulation, we adopted the model mass function of Jung et al. (2021) and the Galaxy model of Jung et al. (2022). Using the assigned physical parameters, we then calculated the corresponding lens observables based on the relations in Eq. (4). Using the simulated events, a Bayesian posterior was derived by constructing the distributions of M and D_L, with each simulated event assigned a weight. The assigned weight was calculated as

$$w_i = \exp\left(-\frac{\chi_i^2}{2}\right); \qquad \chi_i^2 = \left[\frac{t_{E,i} - t_E}{\sigma(t_E)}\right]^2 + \left[\frac{\theta_{E,i} - \theta_E}{\sigma(\theta_E)}\right]^2. \quad (5)$$

Here, (t_E, θ_E) denote the measured lensing observables, while $[\sigma(t_E), \sigma(\theta_E)]$ represent their respective measurement uncertainties. For MOA-2022-BLG-091, for which only a lower limit on the angular Einstein radius, $\theta_{E,min}$, is available, we impose a constraint of $\theta_{E,i} > \theta_{E,min}$.

In Figures 9 and 10, we present the posterior distributions of the lens mass and distance for the events MOA-2022-BLG-091

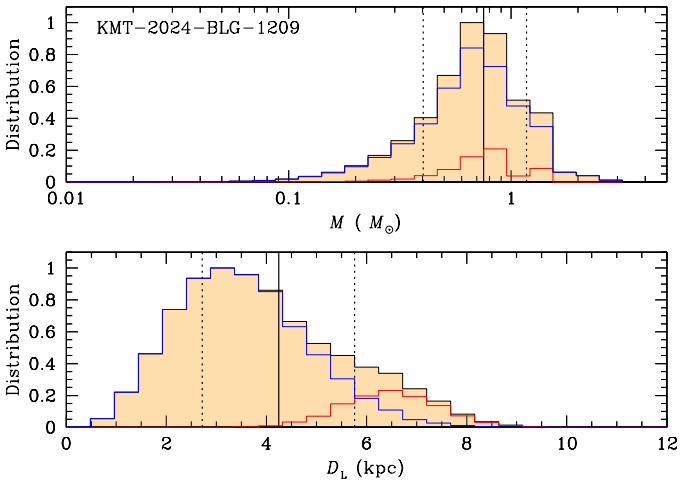

Fig. 10. Posterior of the lens mass and distance for KMT-2024-BLG-1209. Notations are same as those in Fig. 9.

Table 5. Physical lens parameters.

Parameter	MOA-2022-BLG-091		KMT-2024-BLG-1209	
$M_{\rm h}$ ($M_\odot$)	$0.75^{+0.42}_{-0.35}$		$0.77^{+0.46}_{-0.34}$	
$M_{\rm p}$ ($M_{\rm J}$)	$3.59^{+2.00}_{-1.67}$		$2.64^{+1.57}_{-1.16}$	
$D_{\rm L}$ (kpc)	$4.25^{+1.52}_{-1.53}$		$3.93^{+2.03}_{-1.41}$	
$a_\perp$ (AU)	$3.63^{+1.30}_{-1.31}$	(Sol A)	$3.92^{+2.03}_{-1.41}$	(inner)
	$3.44^{+1.92}_{-1.60}$	(Sol B)	$2.51^{+1.50}_{-1.10}$	(outer)
	$2.67^{+1.45}_{-1.24}$	(Sol C)	–	
	$3.26^{+1.80}_{-1.51}$	(Sol D)	–	
$p_{\rm disk}$	87%		86%	
$p_{\rm bulge}$	13%		14%	

and KMT-2024-BLG-1209, respectively. In Table 5, we provide the estimated values for the host and planet masses ($M_{\rm h}$ and $M_{\rm p}$), the distance to the system, and the projected separation of the planet from the host ($a_\perp$). We adopt the median of the posterior distribution as the representative value and define the uncertainty as the range between the 16th and 84th percentiles of the distribution. For each event, we present the values of $a_\perp$ corresponding to the degenerate solutions, which result in different projected separations. The table also includes the probabilities for the planetary system being located in the Galactic disk ($p_{\rm disk}$) or bulge ($p_{\rm bulge}$).

The physical parameters of the two events exhibit similar characteristics in several aspects. First, the planetary companions are giant planets with masses two to four times that of Jupiter in our solar system. Second, the hosts of both planets are main-sequence stars of an early K-type spectral type. Third, the planet is located beyond the host's snow line, which is given by $a_{\rm snow} \sim 2.7\ {\rm AU}(M/M_\odot) \sim 2.0$ AU. Fourth, both planetary systems are very likely to be in the Galactic disk.

8. Summary and conclusion

We analyzed the microlensing events KMT-2022-BLG-0114 and KMT-2024-BLG-1209, whose light curves exhibited anomalies with very similar characteristics. These anomalies, occurring near the peaks of the lensing light curves with moderately high magnifications, are characterized by weak caustic-crossing features with minimal deformation while the source was inside the caustic.

Through detailed modeling of the light curves, we found that the anomalies in both lensing events indicate a planetary origin. These anomalies arose from the source crossing the resonant caustic formed by a planet, with an incidence angle close to a right angle. However, precise interpretation of the anomalies was hindered by various degeneracies. For KMT-2022-BLG-0114, the challenge stemmed from a previously unrecognized degeneracy associated with the uncertainty in the incidence angle of the source's trajectory relative to the planet-host axis. In the case of KMT-2024-BLG-1209, the analysis was complicated by the previously known degeneracy, which results in ambiguity between solutions where the source crosses either the inner or outer side of the caustic relative to the planet host.

The physical parameters of the two planetary systems, estimated through a Bayesian analysis, exhibit similar characteristics in several aspects. In both events, the companions to the lenses are giant planets with masses ranging from two to four times that of Jupiter, and their hosts are early K-type main-sequence stars. Each planet is located beyond the snow line of its host star, and both planetary systems are highly likely to reside in the Galactic disk.

The degeneracy in KMT-2024-BLG-1209 is difficult to resolve due to intrinsic similarities in the caustic structures between the inner and outer solutions. In contrast, the newly identified degeneracy in MOA-2022-BLG-091 arises by chance rather than from inherent features of the caustic itself. Consequently, this degeneracy is expected to be resolved by the upcoming Roman RGES microlensing survey, which will offer higher observational cadence and improved photometric precision from space.

Acknowledgements. This research has made use of the KMTNet system operated by the Korea Astronomy and Space Science Institute (KASI) at three host sites of CTIO in Chile, SAAO in South Africa, and SSO in Australia. Data transfer from the host site to KASI was supported by the Korea Research Environment Open NETwork (KREONET). C.Han acknowledge support from KASI under the R&D program (project No. 2024-1-832-01) supervised by the Ministry of Science and ICT. The MOA project is supported by JSPS KAKENHI Grant Number JP24253004, JP26247023,JP16H06287 and JP22H00153. J.C.Y., I.G.S., and S.J.C. acknowledge support from NSF Grant No. AST-2108414. C.R. was supported by the Research fellowship of the Alexander von Humboldt Foundation. W.Zang acknowledges the support from the Harvard-Smithsonian Center for Astrophysics through the CfA Fellowship. The LCO research uses data obtained through the Telescope Access Program (TAP), which has been funded by the TAP member institutes. This work makes use of observations from the Las Cumbres Observatory global telescope network H.Y., W.Zang, Y.T., S.M. and W. Zhu acknowledge support by the National Natural Science Foundation of China (Grant No. 12133005).

References

Albrow, M. 2017, https://doi.org/10.5281/zenodo.268049
Albrow, M., Horne, K., Bramich, D. M., et al. 2009, MNRAS, 397, 2099
Bensby, T. Yee, J. C., Feltzing, S., et al. 2013, A&A, 549, A147
Bessell, M. S., & Brett, J. M. 1988, PASP, 100, 1134
Bond, I. A., Abe, F., Dodd, R. J., et al. 2001, MNRAS, 327, 868
Chung, S.-J., Han, C., Park, B.-G., et al. 2005, ApJ, 630, 535
Gaudi, B. S, 2012, ARA&A, 50, 411
Gaudi, B. S., & Gould, A. 1997, ApJ, 486, 85
Gould, A. 1992, ApJ, 392, 442
Gould, A., & Loeb, A. 1992, ApJ, 396, 104
Gould, A., Han, C., Zang, W., et al. 2022, A&A, 664, A13
Han, C. 2006, ApJ, 638, 1080
Han, C., Udalsk, A., Gould, A., et al. 2020, AJ, 159, 91
Han, C., Jung, Y. K., & Bond, I. A. 2023, A&A, 675, A36

Han, C., Bond, I. A., Lee, C.-U., et al. 2024a, A&A, 687, A225
Han, C., Albrow, M. D., Lee, C.-U., et al. 2024b, A&A, 689, A209
Han, C., Bond, I. A., Jung, Y. K., et al. 2025, A&A, 694, A90
Hwang, K.-H., Zang, W., Gould, A., et al. 2022, AJ, 163, 43
Johnson, S. A., Penny, M., Gaudi, B. S., et al. 2020, AJ, 160, 123
Jung, Y. K., Han, C., Udalski, A., et al. 2021, AJ, 161, 293
Jung, Y. K., Zang, W., Han, C., et al. 2022, AJ, 164, 262
Jung, Y. K., Hwang, K.-H., Yang, H., et al. 2024, AJ, 168, 152
Kervella, P., Thévenin, F., Di Folco, E., & Ségransan, D. 2004, A&A, 426, 29
Kim, S.-L., Lee, C.-U., Park, B.-G., et al. 2016, JKAS, 49, 37
Kim, H.-W., Hwang, K.-H., Gould, A., et al. 2021, AJ, 162, 15
Kondo, I., Sumi, T., Koshimoto, N., et al. 2023, AJ, 165, 54
Mao, S., & Paczyński, B. 1991, ApJ, 374, 37
Mróz, P., Ryu, Y.-H., Skowron, J., et al. 2018, AJ, 155, 121
Mróz, P., Udalski, A., Bennett, D. P., et al. 2019, A&A, 622, A201
Mróz, P., Poleski, R., Han, C., et al. 2020, AJ, 159, 262
Nataf, D. M., Gould, A., Fouqué, P., et al. 2013, ApJ, 769, 88
Penny, M. T., Gaudi, B. S., Kerins, E., et al. 2019, ApJS, 241, 3
Poleski, R., Suzuki, D., Udalski, A., et al. 2020, AJ, 159, 261
Ryu, Y.-H., Udalski, A., Yee, J. C., et al. 2024, AJ, 167, 88
Sumi, T., Abe, F., Bond, I. A., et al. 2003, ApJ, 591, 204
Udalski, A. 2003, Acta Astron., 53, 291
Udalski, A., Szymański, M. K., & Szymański, G. 2015, Acta Astron., 65
Yang, H., Yee, J. C., Hwang, K.-H., et al. 2024, MNRAS, 528, 11
Yee, J. C., Shvartzvald, Y., Gal-Yam, A., et al. 2012, ApJ, 755, 102
Yee, J. C., Zang, W., Udalski, A., et al. 2021, AJ, 162, 180
Yoo, J., DePoy, D.L., Gal-Yam, A., et al. 2004, ApJ, 603, 13
Zhai, R., Poleski, R., Zang, W., et al. 2024, AJ, 167, 162

[1] Department of Physics, Chungbuk National University, Cheongju 28644, Republic of Korea
[2] Korea Astronomy and Space Science Institute, Daejon 34055, Republic of Korea
[3] Astronomical Observatory, University of Warsaw, Al. Ujazdowskie 4, 00-478 Warszawa, Poland
[4] Institute of Natural and Mathematical Science, Massey University, Auckland 0745, New Zealand
[5] Department of Astronomy and Tsinghua Centre for Astrophysics, Tsinghua University, Beijing 100084, China
[6] University of Canterbury, Department of Physics and Astronomy, Private Bag 4800, Christchurch 8020, New Zealand
[7] Department of Astronomy, Ohio State University, 140 West 18th Ave., Columbus, OH 43210, USA
[8] University of Science and Technology, Daejeon 34113, Republic of Korea
[9] Department of Particle Physics and Astrophysics, Weizmann Institute of Science, Rehovot 76100, Israel
[10] Center for Astrophysics | Harvard & Smithsonian 60 Garden St., Cambridge, MA 02138, USA
[11] School of Space Research, Kyung Hee University, Yongin, Kyeonggi 17104, Republic of Korea
[12] Department of Physics, University of Warwick, Gibbet Hill Road, Coventry, CV4 7AL, UK
[13] Villanova University, Department of Astrophysics and Planetary Sciences, 800 Lancaster Ave., Villanova, PA 19085, USA
[14] Institute for Space-Earth Environmental Research, Nagoya University, Nagoya 464-8601, Japan
[15] Department of Earth and Space Science, Graduate School of Science, Osaka University, Toyonaka, Osaka 560-0043, Japan
[16] Code 667, NASA Goddard Space Flight Center, Greenbelt, MD 20771, USA
[17] Department of Astronomy, University of Maryland, College Park, MD 20742, USA
[18] Department of Earth and Planetary Science, Graduate School of Science, The University of Tokyo, 7-3-1 Hongo, Bunkyo-ku, Tokyo 113-0033, Japan
[19] Instituto de Astrofísica de Canarias, Vía Láctea s/n, 38205 La Laguna, Tenerife, Spain
[20] Institute of Astronomy, Graduate School of Science, The University of Tokyo, 2-21-1 Osawa, Mitaka, Tokyo 181-0015, Japan
[21] Oak Ridge Associated Universities, Oak Ridge, TN 37830, USA
[22] Institute of Space and Astronautical Science, Japan Aerospace Exploration Agency, 3-1-1 Yoshinodai, Chuo, Sagamihara, Kanagawa 252-5210, Japan
[23] Sorbonne Université, CNRS, UMR 7095, Institut d'Astrophysique de Paris, 98 bis bd Arago, 75014 Paris, France
[24] Department of Physics, University of Auckland, Private Bag 92019, Auckland, New Zealand
[25] University of Canterbury Mt. John Observatory, PO Box 56, Lake Tekapo 8770, New Zealand
[26] School of Physics and Astronomy, Tel-Aviv University, Tel-Aviv 6997801, Israel